The annual cycle of energy input, modal excitation and physical plus biogenic turbulent dissipation in a temperate lake

Article

Accepted Version

Simpson, J. H., Woolway, R. I. ORCID: https://orcid.org/0000-0003-0498-7968, Scannell, B. ORCID: https://orcid.org/0000-0001-7627-6327, Austin, M. J. ORCID: https://orcid.org/0000-0003-3179-8767, Powell, B. and Maberly, S. C. ORCID: https://orcid.org/0000-0003-3541-5903 (2021) The annual cycle of energy input, modal excitation and physical plus biogenic turbulent dissipation in a temperate lake. Water Resources Research, 57 (6). e2020WR029441. ISSN 0043-1397 doi: 10.1029/2020WR029441 Available at https://centaur.reading.ac.uk/100086/

To link to this article DOI: http://dx.doi.org/10.1029/2020WR029441

Publisher: American Geophysical Union

Title: The annual cycle of energy input, modal excitation and physical plus biogenic turbulent dissipation in a temperate lake

Authors: John H. Simpson[1], R. Iestyn Woolway[2], Brian Scannell[1],
Martin J. Austin[1], Ben Powell[1], Stephen C. Maberly[3]

Affiliations:
1. Bangor University, School of Ocean Sciences, Menai Bridge, Anglesey, UK
2. European Space Agency Climate Office, ECSAT, Harwell Campus, Didcot, Oxfordshire, UK
3. UK Centre for Ecology & Hydrology, Lancaster Environment Centre, Lancaster, UK

Key points:

1. Increased efficiency of atmospheric energy transfer to a lake during stratification when internal seiche modes are active

2. Dissipation measurements in the bottom boundary layer and pycnocline reveal a biogenic component by migrating organisms

Abstract

A year of measurements by Doppler Current Profilers, a chain of temperature sensors and a suite of meteorological instruments has been analysed to elucidate the seasonal cycle of the dynamical response of a temperate lake (Windermere) to surface forcing. The efficiency of energy input to the lake (*Eff*) was determined by comparing the rate of working by the surface wind-stress *RWy* with the downward flux of momentum in the atmosphere. *Eff* was found to increase from values of ~0.3% in winter mixed conditions, up to ~1.2% during summer stratification, when internal seiches were present. Water column kinetic energy was similarly enhanced during stratification. Spectral analysis of the axial velocity showed that the first vertical mode was dominant during most of the stratified period with a less prominent second mode appearing in the early part of the summer. The observed periods and vertical structure of these modes generally accorded with estimates from internal wave theory based on density profiles. During stratification, pycnocline dissipation exhibited high variability linked to the surface forcing with an average, depth-integrated, pycnocline dissipation rate of $2.5\text{x}10^{-5}$ W m^{-2} corresponding to ~3-4% of *RWy.* Over the same period, the dissipation rate in the bottom boundary layer (BBL) exhibited a marked diurnal variation unrelated to physical forcing. Acoustic backscatter indicated the presence of vertically migrating organisms with peak aggregation in the BBL around midday coinciding with maximum dissipation. During stratification, biogenic dissipation contributed an average of ~36% of the total BBL dissipation rate of ~$5.7\text{x}10^{-5}$ W m^{-2}.

1. Introduction

The seasonal cycle of stratification in lakes results from the interaction between turbulent mixing, forced mainly by surface wind-stress, and surface heat exchange (Fischer et al., 1979;

Imboden and Wüest, 1995). During the spring-summer period, the stratifying effect of surface heat input out-competes vertical mixing, leading to a robust stratified regime developing in all but very shallow polymictic lakes. This stable regime continues until the autumn period, when lakes start to lose heat to the atmosphere and both wind-stress and heat loss act together to erode stratification and induce the autumn overturn. Thereafter a vertically mixed regime prevails through the winter months and continues until surface heat input resumes, around the vernal equinox.

The seasonal cycle of stratification and mixing exerts a major influence on lake biogeochemistry and ecology. For example, stable stratification increases the light received by phytoplankton by reducing the depth of the surface mixed layer and separates zones of primary production in the well-lit epilimnion from zones of decomposition in the darker hypolimnion. This decoupling of processes has consequences for nutrient availability in the epilimnion, oxygen depletion in the hypolimnion and consequent phosphorus release from the sediment and the distribution of organisms within a lake (Yankova et al., 2017). When the water column becomes vertically well-mixed during the autumn overturn, much higher mixing rates prevail, and nutrients are rapidly transported up the water column. These changes in the seasonal mixing regime also affects the vertical transfer rate of other scalar properties including, for example, the potent greenhouse gases carbon dioxide and methane (Vachon et al., 2019).

The general features of the lacustrine seasonal cycle have long been known, principally on the basis of long-term measurements of the temperature structure. New methods for measuring the internal velocity field and estimating the turbulent kinetic energy dissipation rate, ε, over extended periods using Acoustic Doppler Current Profilers (ADCPs) (Antenucci et al., 2000; Simpson et al., 2011), now offer the prospect of more detailed understanding of the rather subtle interaction of the physical processes involved and their impact on the seasonal cycle of lake biogeochemistry and ecology. In a previous, heuristic study in the south basin of Windermere (Woolway and Simpson, 2017), we used a combination of observations with ADCP and temperature chains to examine the input of energy to the lake and its impact on mixing of the density structure and dissipation in the pycnocline and bottom boundary layer (BBL) for a 55-day period covering the spring transition from a mixed to a stratified water column. Here, we have acquired a new, more extensive series of observations with an extended array of ADCPs covering a period of 416 days in a series of five deployments. We have used this unique data set to document the annual cycle of physical processes in the lake and to make quantitative estimates of key physical parameters controlling the cycle of energy input, dissipation and mixing in the lake.

After brief reviews of the observational and analysis methods, which were mostly detailed in Woolway and Simpson (2017), we present the results, starting with an overview of the year-long data set. This is followed by sections based on more detailed analysis of the new data to focus on: (i) determination of the efficiency of energy transfer to the lake by wind stress over the annual cycle, (ii) the changes in the contribution of the internal seiche modes to the response of the lake to wind forcing and (iii) estimates of the levels of energy dissipation and mixing in the pycnocline and the BBL of the lake, both of which exert important controls on lake biogeochemistry.

2. Materials and Methods

2.1 Data collection

The measurements which form the basis of our study, were made in the south basin of Windermere (Fig. S1), which is a long (∼10 km) and narrow (width, <1 km) lake basin situated in the English Lake District, with a surface area of ~6.7 km^2, a maximum depth of 42 m, and a mean depth of 16.8 m. Our observations in Windermere covered the period 20th October 2016 to 11th December 2017 in a series of five deployments of up to 102 days duration (Table S1). Measurements of water motions and density structure were made with a combination of ADCPs and a chain of temperature sensors moored at the location shown in Fig. S1. The water column observations were complemented by measurements of the wind velocity above the lake surface from a raft-mounted meteorological station located close to the moored instruments near the centre of the lake. Measurements of the water column profile of velocity (Fig. S2) were obtained at the lake centre from a bottom-mounted 600 or 300 kHz ADCP (RDI Workhorse) recording average profiles at intervals of $\Delta t = 120$ s based on 50 sub-pings, which were averaged to yield the components of horizontal velocity with a root mean square (rms) uncertainty of ∼1 cm s^{-1} and a vertical bin size of $\Delta z = 1$ m. The velocity profiles extended from ∼2.6 mab (meters above bed) to a level ∼3.5 m below the lake surface. A second Doppler Profiler (1 MHz Nortek Signature or 600 kHz RDI Workhorse) was deployed at a depth of 10 m to sample the near-surface velocity profile in 0.5 or 1 m bins to ∼1.8 m below the surface. Profiles were recorded at 8 Hz in bursts of 175 s at intervals of 2 hours.

High precision velocity data for the determination of turbulent dissipation rate, ε, was obtained using fast sampling ADCPs operating in pulse-pulse (p-p) coherent mode which furnishes low noise data (r.m.s ~1 cm s^{-1}) but with a restricted range (Lhermitte and Serafin, 1984). Because of the long endurance of the deployments (> 100 days) and heavy storage requirements of the turbulence measurements, the duty cycles of the p-p ADCPs were limited to ∼7% of total deployment time. In the BBL, a 1 MHz Nortek Aquadopp profiler, positioned on the lake bed, measured velocity profiles between 0.9 and ∼5 mab with a bin size of 10 cm (Fig. S2). Data was recorded at 2 Hz in 512 s bursts at 120-minute intervals. For the determination of dissipation in the pycnocline, a 600 kHz p-p coherent RDI Workhorse (in mode 11), supported by a buoyant collar, was deployed in midwater to measure velocities over a 7 m vertical span with a bin size of 10 cm. Data bursts of 360 s duration, at intervals of 90 minutes, were measured at 1 Hz with 2 pings per ensemble. Operation in mid-water of a tethered ADCP supported by a buoyant collar has been validated by comparison with shear probe measurements in a previous study (Lucas et al., 2014). A summary of set-up details for the ADCP instruments is provided in Table S2.

The chain of temperature sensors comprised 19 Starmon thermistor microloggers recording every 60 s. The sensors were spaced at intervals of $\Delta z = 2.0$ m above 20 m depth and of $\Delta z = 3.0$ m below. Temperature data was recorded at a resolution of 0.01 °C and an accuracy of ∼0.1 °C. Wind speed and direction were measured at a height of 2.7 m above the lake surface and at time intervals of 240 s by an automatic monitoring station, as described in Woolway and Simpson (2017).

In deployment 1, the midwater p-p ADCP failed completely and some of the other data records were terminated early because of battery and data storage limitations. Since the following deployments, 2-5, provided a data return close to 100%, and covered almost the whole of year 2017, day of year (DOY) 17 to DOY 345, except for breaks of one day for servicing the moorings, we have chosen to treat deployment 1 as our "practice run" and have concentrated the analysis effort on the calendar year 2017.

2.2. Data Analysis

2.2.1. Rate of working by the wind stress

Wind stress inputs energy through the lake surface at a rate which is the product of the stress and the surface velocity. The wind stress components (τ_x, τ_y) acting on the lake surface are determined from the wind observations via the quadratic drag law:

$$(\tau_x, \tau_y) = C_d \rho_a W(U, V) \qquad (1)$$

where C_d is the drag coefficient, calculated as a function of wind speed (Large and Pond, 1981); ρ_a is the air density; U and V are the wind components corrected to anemometer height (Large and Pond, 1981); and W is the wind speed. Assuming that the stress is continuous across the air-water interface, the total rate of working RW by the wind stress components, is given by:

$$RW = RW_x + RW_y = \tau_x u + \tau_y v \qquad (2)$$

where (u, v) are the near-surface velocity components from the uppermost ADCP bin with valid data. Coordinates are rotated so that τ_y and v are directed along the lake axis. To ensure that RW was not greatly biased by using the velocity measurements from the uppermost ADCP bin, rather than velocity from the immediate surface, we compared the velocity shear in the top five ADCP bins, which occupy a ~2 m layer (Fig. S3). Our comparison suggested that within this sub-surface span, the velocity profile is practically uniform, thus supporting our choice of near-surface velocity in the calculation of RW. However, we do acknowledge that the velocity profile is not necessarily above ~1.9 m depth and, indeed, if one assumes a law of the wall similar to the BBL, the velocity could change rapidly when approaching the lake surface.

To determine the efficiency of energy transfer from the atmosphere to lake we compare RW with the rate of working in a horizontal plane above the lake defined by Lombardo and Gregg (1989) as:

$$P10 = C_d \rho_a \overline{|W^3|} \qquad (3)$$

The efficiency of energy transfer, *Eff*, is found by a least squares linear regression of RW on $P10$. Here, the vertical bars indicate the modulus and the overbar denotes the temporal average.

2.2.2. Internal Seiche modes

The periods and modal structure of the internal seiche modes are found by solving the equation for the complex amplitude of the vertical velocity $\psi(z)$ (Gill, 1982):

$$\frac{d^2\psi}{dz^2} + \left(\frac{N^2(z)}{c^2}\right)\psi = 0 \qquad (4)$$

where $N^2 = -\frac{g}{\rho}\frac{\partial \rho}{\partial z}$ is the buoyancy frequency squared derived from the density profile $\rho(z)$ and the boundary condition are $\psi = 0$ at the surface $(z = 0)$ and at the bottom $(z = -h)$. The eigenvalues of this equation for the modes are found numerically following the method of Klink (1999), which are also used to calculate the modal structures $\psi_n(z)$ and the horizontal velocity structure $U_n(z)$. The eigenvalue for mode *n* is the phase velocity c_n which is used to determine the seiche period $T_n = 2L/c_n$ where L is the "effective length" of the basin, i.e., the length of a rectangular basin of constant depth. An initial estimate of L was refined by comparing with the seiche period determined independently by spectral analysis.

2.2.3. Turbulent Kinetic Energy dissipation rate from high resolution velocity measurements

Time series of turbulent kinetic energy (TKE) dissipation rate, ε, are derived from analysis of the along-beam velocities measured by a p-p coherent ADCP using the Structure Function method (Wiles et al., 2006). The raw, along-beam, velocity components $b(x)$ from each beam are used to estimate a second order structure function defined as:

$$D(x,r) = \overline{\left(b'(x) - b'(x+r)\right)^2} \tag{5}$$

where the overbar indicates the mean over a burst of observations and $b' = b(x) - \overline{b}(x)$ is the fluctuating component of velocity at position z along the beam, such that $D(x,r)$ is the mean-square of the along-beam velocity difference between two points separated by a distance r. For isotropic turbulence, the Kolmogorov hypotheses (Kolmogorov, 1941) anticipate that the structure function $D(x,r)$ is related to the dissipation ε by:

$$D(x,r) = C_2 \varepsilon^{2/3} r^{2/3} \tag{6}$$

where C_2 is a constant, for which laboratory studies indicate a value of 2.0 ± 15% (Sreenivasan, 1995). Linear regression of $D(x,r)$ against $r^{2/3}$ yields:

$$D(x,r) = a_0 + a_1 r^{2/3} \tag{7}$$

where $a_0 = 2\sigma_b^2$ is twice the variance of velocity estimates at a point due to instrumental noise of the ADCP and the gradient a_1 is used to derive an ε estimate as:

$$\varepsilon = \left(\frac{a_1}{C_2}\right)^{3/2} \tag{8}$$

Further details of the Structure Function analysis method are given in Text S1.

2.2.4. Seasonal evolution of thermal stratification

As a measure of water column stratification, we use the potential energy anomaly, ϕ (Simpson, 1981), defined as:

$$\phi = \frac{1}{h}\int_{-h}^{0}\left(\bar{\rho} - \rho(z)\right)gz\,dz\,;\ \bar{\rho} = \frac{1}{h}\int_{-h}^{0}\rho(z)dz, \qquad (9)$$

where the density profile $\rho(z)$ is derived from temperature data. ϕ is a measure of the energy required (in J m^{-3}) to fully mix the water column; it is zero in mixed conditions and increases with water column stability.

3. Results

3.1 Overview of the observations

To set the context of the results of the subsequent analysis, we show first, in Fig. 1, plots of the principal environmental parameters of the lake, namely the wind forcing, the temperature structure, the profile of axial flow velocity v along the main axis of the lake basin and the water column Kinetic Energy (KE), together with the dissipation measurements in mid-water and in the BBL. Wind forcing (Fig. 1a) is mainly concentrated in short episodes ($\sim$1 day) separated by longer periods of relative calm. Wind-stress maxima did not exceed 0.5 Pa except during the exceptional storm Ophelia which occurred immediately after the start of deployment 5 when the peak surface stress was $\sim$1 Pa (Woolway et al., 2018).

There was no pronounced seasonal signal in the wind stress during 2017, although averages of $|\tau|$ over the winter period (deployment 2: 0.0364 Pa) were slightly larger than in spring and summer (deployments 3 and 4: 0.0348 Pa). By contrast, the temperature structure (Fig. 1b), follows the relatively smooth, seasonal pattern expected in dimictic temperate lakes, with mixed conditions in winter giving way to stratification soon after the onset of net surface heat input around the vernal equinox at DOY 79; maximum surface temperature occurs, at or soon after, the summer solstice (DOY 172) with strong stratification persisting beyond the autumn equinox (DOY 265) with the resumption of complete vertical mixing at the autumnal overturn. The profile of axial velocity (Fig. 1c), the profile of velocity along the lake's major axis, exhibits a corresponding seasonal pattern with mostly weak flow during the mixed regime in winter followed by more energetic motions after stratification onset and the associated development of internal seiche modes. These motions have a pronounced vertical structure with flow extending to the surface and bed; the strongest flow and vertical shear are frequently located close to the thermocline which separates warm surface waters from the cooler bottom layers. As the thermocline descends, so does the location of the strongest flows until both approach the lake bed in the autumn overturn when complete vertical mixing resumes.

Over the seasonal cycle there is a marked variation in the water column KE at our central observational site. In Fig. 1d, this variation has been separated into depth-uniform KE_{un} and depth varying KE_{va} components defined as:

$$KE_{un} = \frac{1}{2}\rho h\,\langle v\rangle^2\ ;\ KE_{va} = \frac{1}{2}\rho\ \int_{-h}^{0}(v(z) - \langle v\rangle)^2\,dz \qquad (10)$$

where $\langle v\rangle = \frac{1}{h}\int_{-h}^{0} v(z)\,dz$. During the winter period, when the water column is mixed, these two components are of comparable magnitude but, following the transition to a stratified regime, KE_{va} is considerably increased while KE_{un} is little changed. The mean value of KE_{va} (10.8 J m^{-2}) during the early summer stratified regime in deployment 3 (DOY 95-190) exceeds that for the preceding fully mixed winter period during deployment 2 (DOY 17-94) by a factor of ~ 7. In the early part of deployment 4, KE_{va} initially continues at a high level but then declines as stratification weakens towards the end of the year.

The values of the dissipation rate ε (Fig. 1e-f) are averages over the vertical span of the observations (5-7 m and 3.8 m for the midwater and BBL respectively). The vertical span of the midwater observations was set for deployments 3 and 4 to sample dissipation in the pycnocline during stratified conditions. This strategy was most successful during deployment 4 when most of the region of high temperature gradient was covered by the vertical span of the observations. Midwater ε values (Fig. 1e) generally follow the highly variable time course of the wind-stress forcing (Fig. 1a) with a similar pattern of peaks in the two plots. This connection extends through all four deployments shown and is apparent, regardless of whether the water column is stratified or mixed. Midwater ε values range over four decades from the noise level of $\sim 10^{-10}$ W kg^{-1} to peaks up to 10^{-6} W kg^{-1}.

Within the BBL, during deployment 2 when the water column was well-mixed, there was again a considerable degree of matching between peaks in wind-stress and BBL dissipation (Fig. 1f). With the onset of stratification, however, this matching largely disappears and does not return until near the end of deployment 5. During deployments 3 & 4, ε in the BBL exhibited a marked oscillatory form with peak-peak amplitude of up to 10^{-8} W m^{-2}. The origin and significance of this periodic signal is considered in section 3.5.

3.2. Rate of working by the wind stress

We now proceed to determine the rate of mechanical energy input to the lake from the product of the surface stress and the near surface flow, using the approach outlined in section 2.2.1. The wind stress components (τ_x, τ_y), across and along the lake are determined from the quadratic drag law using the wind speed and direction measurements. The surface flow (u_s, v_s) is taken as the velocity, measured by the near-surface doppler in the highest bin with good data (typically 1.6-2.1 m below the lake surface). The axial components of the stress and near surface flow, throughout almost the whole of the year 2017, presented in Fig. 2a-b, are combined to determine their product RW_y, the rate of working in the axial direction. This component dominates over the transverse component RW_x, so that the total $RW \cong RW_y$. For most of the deployment period, RW was positive, i.e., energy is generally being input to the lake flow, with strong positive peaks at times of high wind stress. In the few periods when RW is negative, the surface flow is opposed by the wind stress and KE is being extracted from the lake.

We next examine the variation of the efficiency of energy transfer, *Eff*, from the atmosphere to the lake by comparing RW_y to $P10$, the corresponding rate of working by the wind stress above the lake. Notice in Fig. 2c-d that the peaks of RW and $P10$ generally match closely throughout the year but that the magnitude of RW_y, relative to $P10$, increases sharply following the onset of stratification at around DOY 95, while, at the same time, there is an associated marked increase in the magnitude of the near-surface velocities which persists for ~ 100 days. *Eff* is determined as the slope of a linear, least squares regression of RW_y on $P10$. A series of regressions were performed on 16-day sections of the 2017 data (DOY 17-345) with an overlap of 8 days. The efficiency factor *Eff* plotted in Fig. 2e is the slope of a neutral regression (Garrett and Petrie, 1981). Over the annual cycle, *Eff* varies considerably with levels down to ~0.003 (0.3%) during the mixed regime of winter followed by a sharp increase, soon after the onset of stratification, to a maximum of 1.2%. *Eff* values continue to be high (0.6-1%) through the midsummer period until DOY 200, after which, there is a slow decline and a return to low *Eff* levels as the autumn overturn approaches.

The occurrence of the rapid rise in *Eff* coinciding with the onset of stratification and the persistence, until the autumn overturn, of higher values than those in winter suggest that *Eff* is being enhanced by the presence of stratification which brings with it the availability of internal seiche modes. However, there is a marked asymmetry in the effect of stratification on *Eff* between the spring and autumn transitions: whereas around DOY 90 a value of $\phi\sim$ 2.5 J m^{-3} is enough to trigger the abrupt increase in *Eff*, low values of *Eff* occur for a time after DOY 270, when stratification is still relatively strong ($\phi\sim$ 20 J m^{-3}). The weaker influence of stratification on *Eff* in the autumn may result from changes in the vertical structure of stratification. After DOY 245, the pycnocline weakens and moves further away from the surface in an increasingly rapid descent, which increases the thickness of the epilimnion, changes which modify the structure and frequencies of the seiche modes.

3.3. Internal seiche modes

In this section, we apply spectral analysis to the velocity profiles from the water column ADCP to determine which internal wave modes are active in the response of the lake and to compare the seasonal progression of the modal frequencies with the results of internal wave theory (Text S2). As explained in section 2.2.2, we employ cross-spectral analysis between each ADCP bin level and a reference level near the bed (bin 2 at ~4 mab) for data sections of 21 days which advance by ~5 days to cover each deployment period. Fig. 3a shows an example of a plot of co-spectrum Co versus log (Freq) from all depths from a single 21-day time series (all log values are quoted as $\log_{10}$). In this case, the co-spectra reveal the presence of a strong first vertical mode (v1h1) with a single node centred on a frequency of 0.043 ch^{-1}. There is also a clearly defined second vertical mode (v2h1) at a frequency 0.023 ch^{-1} with 2 nodes.

To illustrate the variation of the modal contributions over the seasonal cycle, the magnitudes of co-spectra $|Co|$ have been summed over the water column between 3 and 37 mab to provide an estimate of the total co-spectral energy at each spectral frequency and time defined as:

$$CoMS(Freq,t)=\sum_{i=1}^{i=34}|Co(i)| \tag{11}$$

The results for $CoMS$ over the whole stratified period are displayed against the log of frequency and time (Fig. 3b). This plot also shows the variation of the frequencies of the first three internal wave modes (v1h1, v2h1 and v3h1) derived from internal wave theory (section 2.2.2) using the square of the buoyancy frequency N^2 based on the density profiles.

A high concentration of mode 1 energy occurs early in deployment 3 as stratification develops and a ridge of high energy follows the trend of the theoretical mode 1 frequency to DOY 145. For the rest of deployment 3, the frequency of the peak response falls below the mode 1 frequency and “clings” to the diurnal frequency, arguably, because of enhanced wind forcing at this frequency (Fig. S4). Then after a period of lighter winds (DOY 165-200), mode 1 re-appears in deployment 4 with its frequency remaining almost constant and in accord with theory at the semi-diurnal frequency for the first half of the deployment period. Thereafter, a weak ridge declines in frequency, but more slowly than indicated by internal wave theory, an effect which may be due to a reduction in the effective length of the lake as the pycnocline descends, acting to slow the decrease of the seiche period.

The second vertical mode also makes a considerable, sustained contribution to the total modal energy from early in deployment 3, when a ridge of energy is seen to follow the theoretical mode 2 frequency into deployment 4 until around DOY 220. After that, there is no clear evidence of mode 2 activity for the rest of the stratified period. As for higher modes, we found no evidence of the excitation of vertical mode 3 or any higher modes contributing significantly to the motion at any time.

Following the recovery and re-deployment of the mooring between deployments 4 and 5, there was an intense, brief episode of wind forcing during Storm Ophelia which induced a sharp change in the density structure (DOY ~289). There were corresponding reductions in the seiche frequency and amplitude which were apparent in a detailed study by Woolway et al., (2018), but not resolved in our 21-day spectral analyses. Thereafter, in deployment 5, there was a period of very limited seiche activity which was only partly attributable to reduced wind forcing. The more general decline in seiche activity seems to be the result of changes in stratification as the pycnocline descended rapidly and the epilimnion increased in thickness while the hypolimnion thinned, changes which apparently diminish the generation of seiche motions. After DOY 320, three bouts of stronger wind forcing, in combination with surface cooling, brought about the autumn overturn and seiche motions disappeared.

3.4. Turbulent dissipation rate in the pycnocline

The pycnocline is the region of enhanced vertical density gradient between the epilimnion and hypolimnion, which develops as the lake stratifies in spring. It forms initially close to the surface and tends to descend as stratification increases. The development of the pycnocline in the south basin of Windermere during the stratified regime of 2017 is illustrated in Fig. 4a by a contoured plot of N^2 averaged over 24 h. Significant stability gradients ($N^2 > 10^{-4}\ \mathrm{s}^{-2}$) are seen to develop in the upper half of the water column soon after DOY 95 with a more intense gradient forming just below the surface and descending rapidly to ~25 mab. Thereafter this pycnocline evolves into a slowly deepening, high gradient interface, with N^2 up to $2.5 \times 10^{-3}\ \mathrm{s}^{-2}$. Between DOY 192 and 275 most of the pycnocline lies within the “pycnocline box”, with vertical span $\Delta \mathrm{z} = 7$ m, within which ε estimates were determined using velocity measurements from the midwater p-p ADCP. We will use these data to characterise pycnocline ε and its relation to RW.

In Fig. 4b-c we show an expanded plot of N^2 in the pycnocline box of deployment 4 pycnocline box together with a corresponding depth-time plot of vertical shear squared $Sh^2 = \left(\frac{\partial u}{\partial z}\right)^2 + \left(\frac{\partial v}{\partial z}\right)^2$ derived from the pycnocline p-p ADCP velocity data and averaged over 24 h. The colour scales are the same for the two plots so that matching colours would correspond to Richardson number of $Ri = N^2/Sh^2$ of order unity. High gradient regions in N^2 and Sh^2 tend to track each other as they descend over time but the occurrence of high Sh^2 is noticeably more intermittent in time than the rather steady progression of N^2. Since the temperature sensors and the ADCP were separated by ~80 m it is not possible to determine accurately the detail of the space-time distribution of Ri but these average plots of N^2 and Sh^2 indicate a pycnocline in a state of marginal stability in which peaks in shear may trigger mixing events.

Figure 5a-b presents the TKE dissipation rate in the pycnocline as $\varepsilon(z,t)$, a function of height in the water column and time and as $\hat{\varepsilon}(t)$ the vertically integrated dissipation rate over the span $\Delta z \sim$6.6 m of the measurements. The observed $\varepsilon(z,t)$ varies over 4 decades with maxima of up to 1x10^{-6} W kg^{-1}. The vertically integrated dissipation rate reached peaks of $\hat{\varepsilon}\sim$1.4 x 10^{-3} W m^{-2} with a mean value in deployment 4 of 2.5 x 10^{-5} W m^{-2}. Dissipation is seen to be highly intermittent with a time course which is clearly related to RWy, the input of energy at the lake surface (Fig. 5c). A regression of $\hat{\varepsilon}$ on RWy, based on 6 hourly means with zero lag, has a slope of 0.019 ± 0.001 which is highly significant with student's t =13.4 and a correlation coefficient 0.56. The corresponding neutral regression slope is 0.034 ± 0.002 which is consistent with the ratio of the means $\bar{\hat{\varepsilon}}/\overline{RWy}$ = 0.033. The maximum correlation coefficient occurs for a lag of 2 hours of $\hat{\varepsilon}$ behind RWy, when r = 0.64 and the neutral regression slope is 0.029± 0.0025.

During the stratified period of deployment 3, the pycnocline box was restricted to 4.8 m in height and less well positioned in relation to the density gradients (Fig. 4) and covers only ~50% of the vertical extent of the pycnocline. Allowing for this yields an estimate of the ratio of the means in the stratified period as $\bar{\hat{\varepsilon}}/\overline{RWy} \approx$ 0.04, which is not inconsistent with the more robust value from deployment 4. The conclusion from this long, continuous time series of pycnocline dissipation is that only a rather small proportion, ~3-4%, of the surface energy input RWy is, on average, dissipated by turbulence in the pycnocline at the centre of the lake. Most of the dissipation in the pycnocline occurs in short, intense bursts. Within the most energetic of these bursts, the criterion for fully isotropic turbulence (Gargett et al., 1984) is satisfied, i.e. the buoyancy Reynold's number $R_b = \varepsilon/\nu N^2$ is $O(10^2)$ or greater (where ν is the kinematic viscosity). At lower values of R_b, anisotropy will act to modify the dissipation estimates although direct numerical simulations (Smyth and Moum, 2000) suggest that, for the structure function method, the isotropic assumption should remain valid down to values approaching $R_b \sim 1$.

In principle, spatially resolved profiles of ε and N^2 should permit estimates of the variation of the vertical diffusivity across the pycnocline using the Osborn (1980) relation $K_z = \Gamma\varepsilon/N^2$ with the efficiency of mixing Γ = 0.2 (Gregg et al., 2018). However, as each estimate of ε uses velocities extending over a span of ±1.9m, the vertical structure is severely smoothed as is evident in Fig. 5. We have, therefore, employed the vertical averages of dissipation $\langle\varepsilon\rangle$ and $\langle N^2\rangle$ in the Osborn relation to estimate the time course of the average diapycnal diffusivity K_z in the pycnocline during deployment 4. The results indicate that mixing in the pycnocline is generally weak except during short-lived maxima of up to $K_z \sim 3$ x10^{-5} m^2 s^{-1}. There is an element of uncertainty in the numerical values of K_z here because of the continuing debate about the appropriate value of the mixing efficiency although recent reviews (Gregg et al., 2018, Monismith et al., 2018) support the use of Γ = 0.2 for the range of Rb in our observations. Note that almost all of the variability in K_z is due to the rapid changes in $\langle\varepsilon\rangle$ which varies over more than 2 orders of magnitude while $\langle N^2\rangle$ (Fig. 5d) declines smoothly from DOY 200 until around DOY 270 when the descending pycnocline starts to exit our pycnocline box. Between DOY 200 and 270, the mean turbulent diffusivity for the period is $\overline{K_z} \approx 10^{-6}$ m^2 s^{-1} which is similar to the value of the kinematic (molecular) viscosity, emphasising the tranquillity of the pycnocline which is stirred significantly only during the infrequent, short bursts of surface forcing.

3.5. Turbulent dissipation rate in the BBL

We noted, in section 3.1, the marked difference between the measured dissipation rates in the BBL and that in the pycnocline. While the latter was clearly responding to forcing by the surface stress (Figs 1e, 5), the plots of BBL dissipation rate during much of the stratified summer regime showed elevated levels that were not linked to wind-stress forcing (Fig. 1f). In Fig. 6a-b we show a more detailed comparison of the depth-integrated, measured dissipation rate $\hat{\varepsilon}$ with RWy during deployment 4 when the time courses of the two variables are seen to be largely unrelated. The most striking feature of the dissipation rate time series is a pronounced periodic variation at the diurnal frequency which is evident through much of the deployment and especially prominent after DOY 235. The vertical structure of the dissipation profile $\varepsilon(z,t)$ (Fig. 6d) reveals that this diurnal signal is often strongest in the upper part of the dissipation profile and, at times, decreases towards the bottom boundary by more than an order of magnitude (e.g., DOY 258-275). This behaviour is the opposite of what would be expected in a seiche-driven boundary layer, in which dissipation should increase towards the bottom boundary. Moreover, in deployment 4, there is no sign of a persistent seiche of a 48-hour period (see Fig. 7) which would be needed to produce a diurnal variation in dissipation.

In search of an explanation for the diurnal modulation of the dissipation rate, we have examined the acoustic backscatter record from the water column ADCP (Fig. 6c) which shows a strong and persistent diurnal pattern characteristic of vertical migration of organisms. Strong backscatter occurs in the upper layers during the hours of darkness and is followed by transfer of the backscattering organisms to the lower half of the water column in time for the daylight hours, when the backscatter signal shows high concentrations extending into the BBL. In order to illustrate the close phase relation between dissipation and the backscatter we show, in Fig. 7a-b an expanded section of the backscatter time series together with the average dissipation in the top 5 bins $\langle\varepsilon_5\rangle$. Maxima in $\langle\varepsilon_5\rangle$ occur consistently during the daytime when the backscatter signal is high near the bed while minima are apparent in the night-time soon after the upward migration, which can be seen in the vertical velocity w measured by the water column ADCP (Fig. 7c). An upward stream of yellow dots on each diurnal cycle indicates organisms swimming upward with velocities of around 1 cm s^{-1}. The swimmers arrive in the near-surface layers ~4 hours before mid-night (indicated by ticks on time axis) and remain there for ~9.5 hours. The downward return migration is not well resolved in the w plot although there are some indications of downward swimming coinciding with the rapid decline of backscatter in the surface layers, e.g., DOY 244-245.

In Fig. 6c there are indications that many, but not all, of the migrators stop in the region of the pycnocline and do not continue further towards the surface. This behaviour is evident in a high concentration band present during night-time which descends from ~28 mab at DOY 210 to ~20 mab by DOY 270. This nightly concentration of organisms in the pycnocline, where they are likely to be feeding, is responsible for a biogenic contribution to pycnocline dissipation which, consequently, varies diurnally. In Fig. 7b pycnocline dissipation is plotted (red line) alongside the contemporary BBL dissipation to reveal that the two are in antiphase as the plankton alternate between pycnocline and BBL. This phase relation provides further confirmation of the role of vertical migration in promoting the diurnal variation of dissipation. The calculated dissipation rates were found to be consistent for a range of maximum separation distances, as detailed in the supplementary information (Text S3; Fig. S5-S6), demonstrating that the observed velocity variances are consistent with the Kolmogorov hypotheses for turbulent flows (Kolmogorov, 1941), rather than arising from a non-turbulent source.

We now proceed to extrapolate the measured vertical distribution of the BBL dissipation rate to (i) extend the observed ε levels from the lowest measured level down to the lake bed and (ii) estimate the proportion of dissipation which can be attributed to the biogenic component. We shall assume that the physically forced dissipation in the BBL is equal to the TKE production in a law of the wall (LOW) boundary layer (Thorpe, 2005) which is given by $\varepsilon_{LOW}(z) = \frac{\rho u_*^3}{\kappa z}$ (W m^{-3}) where u_* is the friction velocity and κ is the von Karman constant. We shall also assume that, at the lowest level measured (z_l = 0.96 mab), the dissipation rate ε_l is primarily due to physical forcing and can be set equal to the LOW value $\varepsilon_l = \frac{\rho u_*^3}{\kappa z_l}$. This second assumption is justified by the rapid decrease in the magnitude of the diurnal (i.e., 'biogenic') component between the highest and lowest Aquadopp bins which can be seen in Fig. 8b. In the second half of the deployment, when the diurnal component is most active, the value in the top bin exceeds that of the lowest bin by 1-2 orders of magnitude.

Integrating from z_0, the bedroughness length, to z_l, we have for the additional depth integrated dissipation rate over the water column below the lowest measured bin:

$$\hat{\varepsilon}_{exd} = \int_{z_0}^{z_l} \frac{\rho u_*^3}{\kappa z} dz = \varepsilon_l z_l \ln\left(\frac{z_l}{z_0}\right) \qquad (12)$$

where $\varepsilon_l = \frac{\rho u_*^3}{\kappa z_l}$ is the observed ε level in the lowest bin. The total depth-integrated dissipation rate in the BBL up to z_u, the height of the highest bin measured, is then:

$$\hat{\varepsilon}_{tot} = \hat{\varepsilon}_{meas} + \hat{\varepsilon}_{exd} \quad [\mathrm{W\ m^{-2}}] \qquad (13)$$

where $\hat{\varepsilon}_{meas}$ is the depth integral of the dissipation in the measured bins. The plot of $\hat{\varepsilon}_{tot}$ (Fig. 8c) exhibits a reduced diurnal component relative to $\hat{\varepsilon}_{meas}$ (Fig. 8a) because the extrapolated component $\hat{\varepsilon}_{exd}$ is based only on the measurement in the lowest bin where the diurnal component is much weaker. We can also extrapolate upwards from z_l to make an estimate of the dissipation which would occur between z_l and z_u in a LOW boundary layer without inputs from biogenic sources:

$$\hat{\varepsilon}_{exu} = \int_{z_l}^{z_u} \frac{\rho u_*^3}{\kappa z} dz = \varepsilon_l z_l \ln\left(\frac{z_u}{z_l}\right) \qquad (14)$$

An estimate of the biogenic input between z_l and z_u is then:

$$\hat{\varepsilon}_{bio} = \hat{\varepsilon}_{meas} - \hat{\varepsilon}_{exu} \tag{15}$$

We also have the total physical dissipation in the LOW boundary layer below z_u as:

$$\hat{\varepsilon}_{LOW} = \int_{z_o}^{z_u} \frac{\rho u_*^3}{\kappa z} dz = \varepsilon_l z_l \ln\left(\frac{z_u}{z_0}\right) = \hat{\varepsilon}_{exd} + \hat{\varepsilon}_{exu} \tag{16}$$

The result of the extrapolation procedures has been to divide the total BBL dissipation $\hat{\varepsilon}_{tot}$ into a physically driven component $\hat{\varepsilon}_{LOW}$ below 4.7 mab (Fig. 8c) and a biogenic component $\hat{\varepsilon}_{bio}$ between 0.9 and 4.7 mab (Fig. 8e).

Physically driven dissipation was generally weak as would be expected from the low level of RWy (Fig. 6a) during most of deployment 4. Nevertheless, during the first half of the deployment, $\hat{\varepsilon}_{LOW}$ makes a mostly larger contribution to $\hat{\varepsilon}_{tot}$ than $\hat{\varepsilon}_{bio}$, notably in events like those at DOY 206 and 228 with peaks of ~3.5 x 10^{-4} W m^{-2}, which are clearly linked to wind-stress forcing. By contrast, after DOY 235, $\hat{\varepsilon}_{bio}$ becomes much more active with large diurnal oscillations ranging from peaks of up to ~4.5 x 10^{-4} W m^{-2} down to minima of ~10^{-6} W m^{-2}; over the period DOY 240-280, the mean ε_{bio} was ~1.8 x 10^{-5} W m^{-2}. The same extrapolations procedures were applied to the BBL dissipation rate measurements obtained during deployment 3 when surface energy input RWy was ~40% higher than during deployment 4. The average depth-integrated dissipation rate components for the two deployments are compared in Table S3. The results for the two deployments are generally rather similar but reflect the higher energy input during deployment 3. Over the combined 200 day period of deployments 3 & 4, the average biogenic dissipation, $\bar{\hat{\varepsilon}}_{bio}$, amounted to 36% of the total dissipation in the BBL. In the same period, physically-forced dissipation in the BBL was ~4% of RWy, the energy input at the surface by wind-stress.

4. Summary and Discussion

The analysis of the year-long dataset has resulted in the following principal conclusions:

i) The efficiency of mechanical energy transfer from the atmosphere to the lake by wind-stress varies over the seasonal cycle, by a factor of ~4, between a maximum of ~1.2% soon after the onset of stratification and ~0.3% in unstratified conditions.

ii) There is a corresponding cycle in the water column KE with peak values early in the stratified regime greater than those of the mixed regime by a factor of ~7. This increase in KE occurs only in the depth varying component and continues, with a slow decline, until the autumn overturn.

iii) There is a well-defined seasonal pattern in the observed frequency of the dominant lowest vertical mode seiche (v1h1) which tracks close to that given by internal wave theory. In the early summer, there was clear evidence of an active second vertical mode (v2h1), whose frequency also follows internal wave theory. There was no evidence of mode 3 or any higher modes being excited.

iv) TKE dissipation rate in the mature summer pycnocline varied widely (ε = 10^{-10} to 10^{-6} W kg^{-1}) and was closely correlated to surface forcing. On average, total dissipation in the pycnocline accounted for 3-4% of RW_y, while vertical average diffusivity in the pycnocline was limited to maximum values of up to $K_z \sim 3 \times 10^{-5}\ \mathrm{m^2 s^{-1}}$ occurring in short bursts.

v) Dissipation in the BBL for the summer period was much less influenced by wind stress forcing and exhibited a strong semi-diurnal variation. Acoustic back-scatter data indicated the presence of vertically migrating organisms on a diurnal cycle in which the migrants were present near the bed during the daylight hours when BBL dissipation levels increased by up to two orders of magnitude.

vi) The maximum concentration of organisms in the BBL occurred consistently in phase with the dissipation in the diurnal cycle while measurements of the vertical velocity indicated organisms swimming upward at a velocity of ~1 cm s^{-1} and arriving in the surface layers ~4 hours before midnight.

vii) Many of the swimmers appeared to remain in the pycnocline for several hours where they induced a biogenic contribution to the dissipation rate, which varied diurnally, in phase with the concentration of organisms, and in antiphase with the dissipation rate in the BBL (Fig. 7b).

viii) During the stratified period, the total BBL dissipation rate below 5 m averaged 5.7 x 10^{-5} W m^{-2}, made up of a physical, LOW boundary layer contribution of ~64% with the remaining ~36% coming from biogenic input.

ix) Combined physically-forced dissipation in the pycnocline and the BBL amounted to 5.6-9.0% of RWy.

The marked change in the efficiency of energy transfer from the atmosphere with the onset of stratification in our observations is consistent, in timing and magnitude, with the abrupt increase in *Eff* observed during the spring transition in 2013 (Woolway and Simpson, 2017). Together with the continuing pattern of enhanced *Eff* through mid-summer 2017 and into the autumn, these findings support the hypothesis that internal seiche modes promote energy transfer during the stratified regime and build the high levels of water column KE observed in summer. Further supportive evidence can be seen in the pattern of modal activity in the stratified period (Fig. 6b) which is similar to that of the variation of *Eff* with a strong response at the onset of stratification and continuing through the mid-summer period before declining in autumn.

It is also probable that the development of a low-friction layer in the pycnocline helps to facilitate the growth of seiches by acting to decouple the epilimnion from the hypolimnion and, thus, promote stronger flows in the surface layer which increases the pycnocline slope which, in turn, forces an enhanced response in the hypolimnion and energises the lake. In late summer, there is a significant decline in *Eff* which may be attributed to a weaker response of pycnocline slope to wind-stress caused by the thickening of the epilimnion as the pycnocline deepens. This mechanism may also explain the weak response of seiche motions during the approach to the autumnal overturn during deployment 5.

There are rather few previous reported studies of energy input to lakes and only one, as far as we know, which includes an estimate of *Eff*. On the basis of a series of temperature microstructure measurements in Alpnacher See (Switzerland), Wüest et al., (2000) estimated that, in stratified conditions, ~0.7% of $P10$ was dissipated, or used in mixing, below the surface layer (6 m depth), an estimate which is consistent with the average of our estimates for the stratified regime of $\overline{Eff} = 0.70\% \pm 0.23\%$.

The spectral analysis of the axial flow in the centre of the lake provides, arguably for the first time, a clear picture of the seasonal progression of modal activity in the velocity field during stratification. The first vertical mode is clearly dominant for most of the time and has a frequency which varies with the evolving stratification in accord with internal wave theory. The first mode response is particularly strong when its frequency is close to that of diurnal wind-stress forcing (Fig. S4). During the early part of the summer, a generally weaker, second vertical mode was also evident at frequencies which again were in accord with theory; no higher modes contributed significantly to the co-spectra. This picture is in broad accord with many previous observations of seiches in temperate lakes comparable to Windermere (Stevens et al., 1996; Lemmin et al., 2005) which mostly show a predominance of the first vertical mode with some additional contribution from the second mode. A clear example of a dominant second vertical mode was observed by Münnich et al., (1992) in the Alpnacher See when there was a substantial metalimnion and the frequency of the second mode matched that of the diurnal wind forcing. One might expect a similar matching to local forcing to promote seiche modes higher than 2, however, the report by Vidal and Casamitjana (2008) of mode 3 seiches in the Sau reservoir (Spain) is one of the few examples in the literature.

In spite of the key role of pycnocline dissipation and mixing in the biogeochemistry of lakes, few measurements have been reported in the literature to date. Of these, most have been made using free-fall shear probes and/or temperature microstructure profilers (Imberger and Ivey, 1991; Stevens et al., 2005) both of which are labour intensive and are not suited to long time series of continuous observations. The results of the present study have demonstrated that p-p Doppler profilers, tethered in the pycnocline, combined with Structure Function analysis can provide a straightforward and effective methodology for long term observations of dissipation in all weather conditions. In view of the paucity of existing measurements of TKE dissipation and mixing coefficients in the pycnocline, there would seem to be a strong case for further application of the methods used in this study. Future long-term measurements of this kind might usefully be combined with the complementary approach of Preusse et al., (2010), who used high resolution thermistor chains in Lake Constance to determine pycnocline dissipation via a Thorpe scale analysis of density instabilities.

The most surprising results of this study have come from the dissipation rate measurements in the BBL which exhibited a pronounced diurnal variation with ε, at times, increasing with height above the bed. Neither of these features are consistent with dissipation produced by a purely physical process and we have been forced to examine the idea that a component of the dissipation was being driven by diurnal migration of organisms whose presence was clearly indicated by a regular diurnal pattern in the echo-intensity signal from the bottom-mounted ADCP monitoring flow in the water column. Many aquatic organisms perform diurnal vertical migrations for a variety of reasons that trade-off the costs and benefits of conditions in the epilimnion and hypolimnion for metabolic rates, food availability and predation pressure (Lampert, 1989; Loose & Dawidowitz, 1994). There is a tendency for a greater abundance of fish and zooplankton in surface waters at night and a lesser abundance during the day but there is a large variability of movement patterns depending on species and life stage (Scofield et al. 2020) and some species move horizontally from the pelagic during the night to the littoral at day rather than vertically. Within Windermere, hydroacoustic surveys show that Arctic charr and other fish are more abundant in the surface waters at the night than at the day (Elliott & Baroudy 1992; Winfield & Fletcher 2007). Work on the North Basin of Windermere, which is deeper than the South Basin, in the 1950s (Colebrook, 1960) showed substantial vertical migration for several species of zooplankton. For example, in June 1956, stages IV and V of *Arctodiaptomus laticeps* were below 40 m depth during the day but predominantly above 10 m depth at night. *Eudiaptomus gracilis* was also distributed largely in the top 10 m at night but showed lesser and variable migration to depth during the day depending on stage and sex. In another campaign in autumn 1955, *Cyclops strenuous* males also performed diurnal vertical migration, being absent from the surface during the day while accumulating between 15 and 30 m depth. Thus, the well-known patterns of diurnal vertical migration of fish and especially zooplankton, that also occur in Windermere, are consistent with the acoustic backscatter data shown in our study. The estimated rates of swimming are also consistent with measured swimming speeds of zooplankton which can exceed 1 cm s^{-1} depending on species and conditions (Ekvall et al. 2020).

The close phase relation between the BBL dissipation rate and the echo signal with maximum dissipation occurring when migrators were present in the BBL, strongly supports the hypothesis that migrating organisms were contributing to BBL dissipation. Further support comes from the pycnocline measurements which indicate a diurnally varying, biogenic component which varies in antiphase with the BBL dissipation rate. A first-order separation of the biogenic and physical sources of dissipation in the BBL, obtained by extrapolating downwards and upwards from the lowest Doppler bin using the law of the wall, indicated that the biogenic component accounted for an average of ~36% of the total BBL dissipation rate during the stratified regime.

Biogenic mixing in the ocean has been widely reported in the literature, but there are only a few studies related to mixing in lakes (Noss and Lorke, 2014; Simoncelli et al., 2017; Simoncelli et al., 2018). The only report of measured values of biogenic dissipation in the lacrustine environment is, as far as we know, the recent paper of Sepulveda Steiner et al., (2021) who observed a 1 m-thick mixed-layer driven by bioconvection due to vertically migrating bacteria in a stratified lake. Our serendipitous observations of a very different bio-turbulence scenario, in Windermere, will, we trust, stimulate further investigations of bio-turbulence in lakes, where the generally low levels of physically-driven turbulence, can make modest biogenic inputs, of the type we have observed, important in promoting mixing. There are some obvious limitations in our study which was planned to investigate only physical aspects of the seasonal cycle, so there was no net sampling of the plankton to establish the plankton species involved and their behaviour. From past sampling programmes in Windermere (as described above), it seems likely that the zooplankton responsible for generating the biogenic contribution to turbulent dissipation, which we have observed, are copepods of unknown species. It is their swimming activity which generates the bio-turbulence but their regular vertical migration which strongly modulates turbulence levels in the BBL and, to a lesser degree, in the pycnocline, which provided us with a helpful guide to their presence and activity.

There is also an interesting question about whether the scales of turbulence, produced by swimming zooplankton swimming, are too small to bring about significant mixing. In experiments with large concentrations of zooplankton in laboratory tanks, Houghton et al., (2018) have demonstrated that migrating aggregations of organisms can produce large-scale mixing eddies as a result of flow, in the wakes of individual organisms, coalescing to form a large-scale downward jet during upward swimming, even in the presence of a strong density stratification. Our observations, which rely on the structure function determination of turbulent velocity differences over scales greater than 2 bins (20 cm), also suggest that such relatively large-scale eddies are indeed produced by zooplankton stirring. This conclusion is further supported by trial evaluations of ε for a range of r_{max} values between 1 and 3 m which indicates minimal dependence on the maximum separation distance (Text S3; Fig. S5).

Acknowledgements

We acknowledge with thanks the contributions of Ben James (UK Centre for Ecology & Hydrology, Lancaster) and Natasha Lucas (SOS, Bangor) in the deployment and recovery of the instrument array in Windermere. Cumbrian Lakes data and infrastructure were supported by Natural Environment Research Council award number NE/R016429/1 as part of the UK-SCaPE programme delivering National Capability. BDS was supported by NERC award 1500369 through the Envision Doctoral Training Programme. **Data availability statement:** All observational data used in this study are available at https://zenodo.org/record/4785030#.YMNFUC2ZNAY.

References

Antenucci, J.P., Imberger, J. & Saggio, A. (2000). Seasonal evolution of the basin-scale internal wave field in a large stratified lake. *Limnol. Oceanogr.* 45, 1621–1638

Colebrook, J.M. (1960). Plankton and water movements in Windermere. *Journal of Animal Ecology* 29(2), 217-240

Ekvall, M. et al. (2020). Behavioural responses to co-occurring threats of predation and ultraviolet radiation in Daphnia. *Freshwater Biol* 65, 1509-1517

Elliott, J.M. & Baroudy, E. (1992), Long-term and short-term fluctuations in the numbers and catches of Arctic charr, Salvelinus alpinus (L.), in Windermere (northwest England). *Annls Limnol*. 28, 135-146

Fischer, H.B., List, E. J., Koh, R. C. Y., Imberger, J. & Brooks, N.H. (1979). Mixing in Inland and Coastal Waters. Academic Press, London.

Gargett A.C., Osborn, T.R. & Nasmyth, P.W. (1984). Local isotropy and the decay of turbulence in a stratified fluid. *J. Fluid Mech*.144, 231-280

Garrett, C., Petrie, B. (1981). Dynamical aspects of the flow through the strait of Belle Isle. *J. Phys. Oceanogr.* 11, 376-393.

Gill, A.G. (1982). Atmosphere-ocean dynamics. *Int. Geophys. Ser.* 30, 159–162.

Gregg, M.C. et al. (2018). Mixing efficiency in the ocean. Annual Review of Marine Science 10, 443-473.

Houghton, I.A., Koseff, J.R., Monismith, S.G., Dabiri, J.O. (2018). Vertically migrating swimmers generate aggregation-scale eddies in a stratified column. *Nature*. 556, 497–500

Imberger, J. & Ivey, G.N. (1991). On the nature of turbulence in a stratified fluid. Part II: Application to lakes. *J. Phys. Oceanogr.* 21, 659–680.

Imboden, D.M. & Wüest, A. (1995). Mixing mechanisms in lakes. In: Physics and chemistry of Lakes. Springer, pp 83–138.

Klink, J. (1999). Dynmodes.m—ocean dynamics vertical modes. Woods Hole (MA): Woods Hole Science Center, SEA-MAT, Matlab tools for oceanographic analysis. Available from: http://woodshole.er.usgs.gov/operations/sea-mat/index.html

Kolmogorov, A.N. (1941). Dissipation of energy in the locally isotropic turbulence. *Dokl. Akad. Nauk SSSR*, 32, 19-21

Lampert, W. (1989). The Adaptive Significance of Diel Vertical Migration of Zooplankton. *Functional Ecology* 3, 21-27

Large, W.G. & Pond, S.S. (1981). Open ocean momentum flux measurements in moderate to strong winds. *J. Phys. Oceanogr*. 11, 324–336

Lemmin, U., Mortimer, C.H., Bäuerle, E. (2005). Internal seiche dynamics in Lake Geneva. *Limnol. Oceanogr.* 50(1), 207-216

Lhermitte, R. & Serafin, R. (1984). Pulse-to-pulse coherent Doppler sonar signal processing techniques. *J. Atmos. Oceanic Technol.* 1, 293–308.

Lombardo, C.P. & Gregg, M.C. (1989). Similarity scaling of viscous and thermal dissipation in a convecting surface boundary layer. *J Geophys. Res-Oceans* 94, 6273–6284.

Loose, C.J. & Dawidowitz, P. (1994), Trade-Offs in Diel Vertical Migration by Zooplankton: The Costs of Predator Avoidance. *Ecology* 75(8), 2255-2263

Lucas, N., Simpson, J.H., Rippeth, T.P. & Old, C. (2014). Measuring dissipation via the structure function using a tethered ADCP. *J Atmos. Oceanic Technol.* 31, 1826–1837

Monismith, S.G., Koseff, J.R. & White, B.L. (2018). Mixing efficiency in the presence of stratification: When is it constant? *Geophys. Res. Lett*. **45**, 5627–5634

Münnich, M.A., Wüest, A. & Imboden, D.M. (1992). Observations of the second vertical mode of the internal seiche in an alpine lake. *Limnol. Oceanogr*. 37, 1705–1719. doi:10.4319/lo.1992.37.8.1705

Noss, C. & Lorke, A. (2014). Direct observation of biomixing by vertically migrating zooplankton. *Limnol. Oceanogr*. 59(3), 724-732.

Osborn, T. R. (1980). Estimates of the local rate of vertical diffusion from dissipation measurements. *J. Phys. Oceanogr.* 10, 83-89.

Preusse, M., Peeters, F. & Lorke, A. (2010). Internal waves and the generation of turbulence in the thermocline of a large lake. *Limnol. Oceanogr*. 55(6), 2353– 2365.

Scofield, A.E. et al. (2020). Heterogeneity in zooplankton distributions and vertical migrations: Application of a laser optical plankton counter in offshore Lake Michigan. *J. Great Lakes* Res 46(4), 780-797

Simoncelli, S., Thackeray S. & Wain, D. (2017). Can small zooplankton mix lakes? *Limnol. Oceanogr. Lett*. 2(5):167–176.

Simoncelli, S., Thackeray, S.J., Wain, D.J. (2018). On biogenic turbulence production and mixing from vertically migrating zooplankton in lakes. *Aquat. Sci*. 80:35.

Simpson, J.H. (1981). The shelf-sea fronts: Implications of their existence and behaviour. *Philos. Trans. R. Soc. Lond*. 302, 531–546. doi:10.1098/rsta.1981.0181

Simpson, J.H., Wiles, P.J. & Lincoln, B.J. (2011). Internal seiche modes and bottom boundary-layer dissipation in a temperate lake from acoustic measurements. *Limnol. Oceanogr.* 56, 1893–1906. doi:10.4319/lo. 2011.56.5.1893

Smyth, W.D. & Moum, J.N. (2000). Anisotropy of turbulence in stably stratified mixing layers. *Phys. Fluids*. 12(6), 1343-1362.

Sreenivasan, K.R. (1995). On the universality of the Kolmogorov constant. *Phys. Fluids*. 7, 2778-2784

Sepúlveda Steiner, O., Bouffard, D. & Wüest, A. (2021), Persistence of bioconvection-induced mixed layers in a stratified lake. Limnol Oceanogr. https://doi.org/10.1002/lno.11702

Stevens C.L., Fisher T.S.R. & Lawrence G.A. (2005). Turbulent layering beneath the pycnocline in a strongly stratified pit lake. *Limnol. Oceanogr*., 50(1), 197–206.

Stevens, C., Lawrence, G., Hamblin, P. & Carmack, E. (1996). Wind forcing of internal waves in a long narrow stratified lake. *Dyn. Atmos. Oceans*, 24, 41–50

Thorpe, S.A. (2005). The Turbulent Ocean, Cambridge University Press.

Vachon, D. et al. (2019). Influence of water column stratification and mixing patterns on the fate of methane produced in deep sediments of a small eutrophic lake. *Limnol. Oceanogr.* 64(5):2114-2128.

Vidal, J. & Casamitjana, X. (2008). Forced Resonant Oscillations as a Response to Periodic Winds in a Stratified Reservoir. *J. Hydraul. Eng*. 134(4), 416-425.

Wiles P.J., Rippeth, T.P., Simpson, J.H. & Hendricks, P.J. (2006). A novel technique for measuring the rate of turbulent dissipation in the marine environment. *Geophys. Res. Lett*. 33: L21608. doi:10.1029/2006GL027050.

Winfield, I.J., Fletcher, J.M. & James, J.B. (2007). Seasonal variability in the abundance of Arctic charr (Salvelinus alpinus (L.)) recorded using hydroacoustics in Windermere, UK and its implications for survey design. *Ecology of Freshwater Fish* 16(1), 64-69

Woolway, R.I. & Simpson, J.H. (2017). Energy input and dissipation in a temperate lake during the spring transition. *Ocean Dynamics* 67, 959–971. doi 10.1007/s10236-017-1072-1

Woolway, R.I., Simpson, J.H., Spiby, D., Feuchtmayr, H., Powell, B. & Maberly, S.C. (2018). Physical and chemical impacts of a major storm on a temperate lake: a taste of things to come? *Climatic Change* 151, 333-347. doi: 10.1007/s10584-018-2302-3.

Wüest, A., Piepke, G., Van Senden, D.C. (2000). Turbulent kinetic energy balance as a tool for estimating vertical diffusivity in wind-forced stratified waters. *Limnol. Oceanogr*. 45, 1388–1400. doi:10.4319/lo.2000.45.6.1388

Yankova, Y. et al., (2017). Abrupt stop of deep water turnover with lake warming: Drastic consequences for algal primary producers. *Sci. Rep*. **3**:13770

References from Supporting Information

Emery, W.J. & Thomson, R.E. (1998). Data analysis methods in physical oceanography. *Oceanographic Literature Review* 1, 45.

Scannell, B., Rippeth, T.P., Simpson, J.H., Polton, J.A. & Hopkins, J.E. (2017). Correcting Surface Wave Bias in Structure Function Estimates of Turbulent Kinetic Energy Dissipation Rate*. J. Atmos. Oceanic Technol.* 34, 2257-2273

Ramsbottom, A.E. (1976). Depth charts of the Cumbrian Lakes. *Freshw. Biol. Assoc. Sci. Publl.* 33

List of Figures

Figure 1. Overview of observations in deployments 2 to 5 in Windermere during the 2017 campaign. **(a)** Wind stress magnitude τ (Pa); **(b)** Temperature (°C); **(c)** Water column velocity v, measured between ~3 metres above bed (mab) and ~37 mab; **(d)** Water column kinetic energy (KE) components: KE_{un} (black) and KE_{va} (red), based on the depth-average and depth-varying axial velocity, respectively; **(e)** Depth-mean dissipation rate (W kg^{-1}) measured in a vertical span of 6.6 m (4.9 m in deployment 3); span depth was located in the pycnocline during the stratified regime (deployments 3 and 4); **(f)** Depth-mean dissipation rate (W kg^{-1}) in the bottom boundary layer (BBL) between 0.96 and 4.66 mab.

Figure 2. Rate of working and efficiency of energy transfer, *Eff*, through the lake surface. **(a)** axial wind-stress τ (Pa); **(b)** near-surface axial velocity v_s (m s^{-1}) measured at 1.6-2.1 m below the lake surface and averaged over 20 minutes; **(c)** RW_y (W m^{-2}) the rate of working just below the lake surface by the axial wind-stress (mean depth ~1.9m); **(d)** the rate of working in the atmosphere at anemometer height of 10m (P10, W m^{-2}); **(e)** Eff based on regression of RW_y on P10 for 16-day data sections; 95% confidence bounds in red; **(f)** Potential energy anomaly ϕ (J m^{-3}).

Figure 3. Spectral analysis of internal wave motions. **(a)** Co-spectrum between axial velocity at each bin level and that at 3.6 metres above bed (mab) for day of year (DOY) 147-168. **(b)** Vertical sum of co-spectrum magnitude ($CoMS$) versus time and log frequency. Line plots show the variation of modal frequencies based on internal wave theory with observed density profiles: mode 1 (magenta), mode 2 (red) and mode 3 (grey). Dashed white lines indicate diurnal and semi-diurnal periods. The Co-spectrum is the in-phase component of the Cross-spectrum.

Figure 4. Pycnocline structure and shear. **(a)** Contours of daily means of N^2 (s^{-2}) derived from density profiles averaged over 24 h. White boxes indicate the extent of the pycnocline dissipation measurements during deployments 3 and 4. **(b)** Expanded plot of N^2 for the deployment 4 pycnocline box. **(c)** Corresponding plot of Sh^2 (s^{-2}) derived from pycnocline p-p ADCP data. Lake profiles are shown relative to metres above bed (mab).

Figure 5. Dissipation (ε) and diffusivity (K_z) in the pycnocline during deployment 4. Log plots versus day of year (DOY) of **(a)** Vertical structure of $\varepsilon(z,t)$ (W kg^{-1}) in a 6.6 m span of the pycnocline relative to metres above bed (mab); **(b)** Vertically integrated dissipation $\hat{\varepsilon}(t)$ (W m^{-2}) over same span; **(c)** Rate of working near the surface by axial wind-stress RWy (W m^{-2}); **(d)** Stability frequency squared N^2(s^{-2}); **(e)** Vertical diffusivity K_z (m^2 s^{-1}).

Figure 6. Bottom boundary layer (BBL) dissipation and echo intensity during deployment 4. **(a)** Rate of energy input at the lake surface RWy (W m^{-2}); **(b)** Depth integrated, measured dissipation rate, $\hat{\varepsilon}_{meas}(t)$ (W m^{-2}), between 0.96 and 4.66 metres above bed (mab); **(c)** Backscatter intensity, BS (dB) from bottom mounted ADCP covering water column from 3.7

to 36 metres above bed (mab) **(d)** Vertical structure of the dissipation rate $\varepsilon(z, t)$ (W kg^{-1}) in the BBL. Black rectangle shows the 7-day period of the expanded region in Fig. 7.

Figure 7. Expanded plots for day of year (DOY) 240-247 of **(a)** the acoustic backscatter intensity, BS from the water column ADCP (black box in Fig. 6) relative to metres above bed (mab), **(b)** the mean dissipation (W kg^{-1}) in the top five Aquadopp bins $\langle\varepsilon_5\rangle$ (blue) and in the pycnocline $\langle\varepsilon_{pyc}\rangle$ (red), and **(c)** the vertical velocity w (m s^{-1}) from the water column ADCP. Note that on the time axis, the larger ticks denote the times of midnight (UT).

Figure 8. Extrapolation of dissipation in the bottom boundary layer (BBL). **(a)** $\hat{\varepsilon}_{meas}$ the integrated measured dissipation between 0.96 and 4.66 metres above bed (mab) in the BBL. **(b)** ε_{bin} : dissipation rate (W kg^{-1}) in the highest bin (red, 4.66 mab) and in the lowest bin (black, 0.96 mab) of the Aquadopp span. **(c)** $\hat{\varepsilon}_{tot} = \hat{\varepsilon}_{meas} + \hat{\varepsilon}_{exd}$: total dissipation in the BBL up to 4.66 mab. **(d)** $\hat{\varepsilon}_{LOW} = \hat{\varepsilon}_{exd} + \hat{\varepsilon}_{exu}$: estimate of physical dissipation in the BBL up to 4.66 mab. **(e)** $\hat{\varepsilon}_{bio} = \hat{\varepsilon}_{meas} - \hat{\varepsilon}_{exu}$ estimate of the biogenic component of dissipation between 0.96 mab and 4.66 mab.

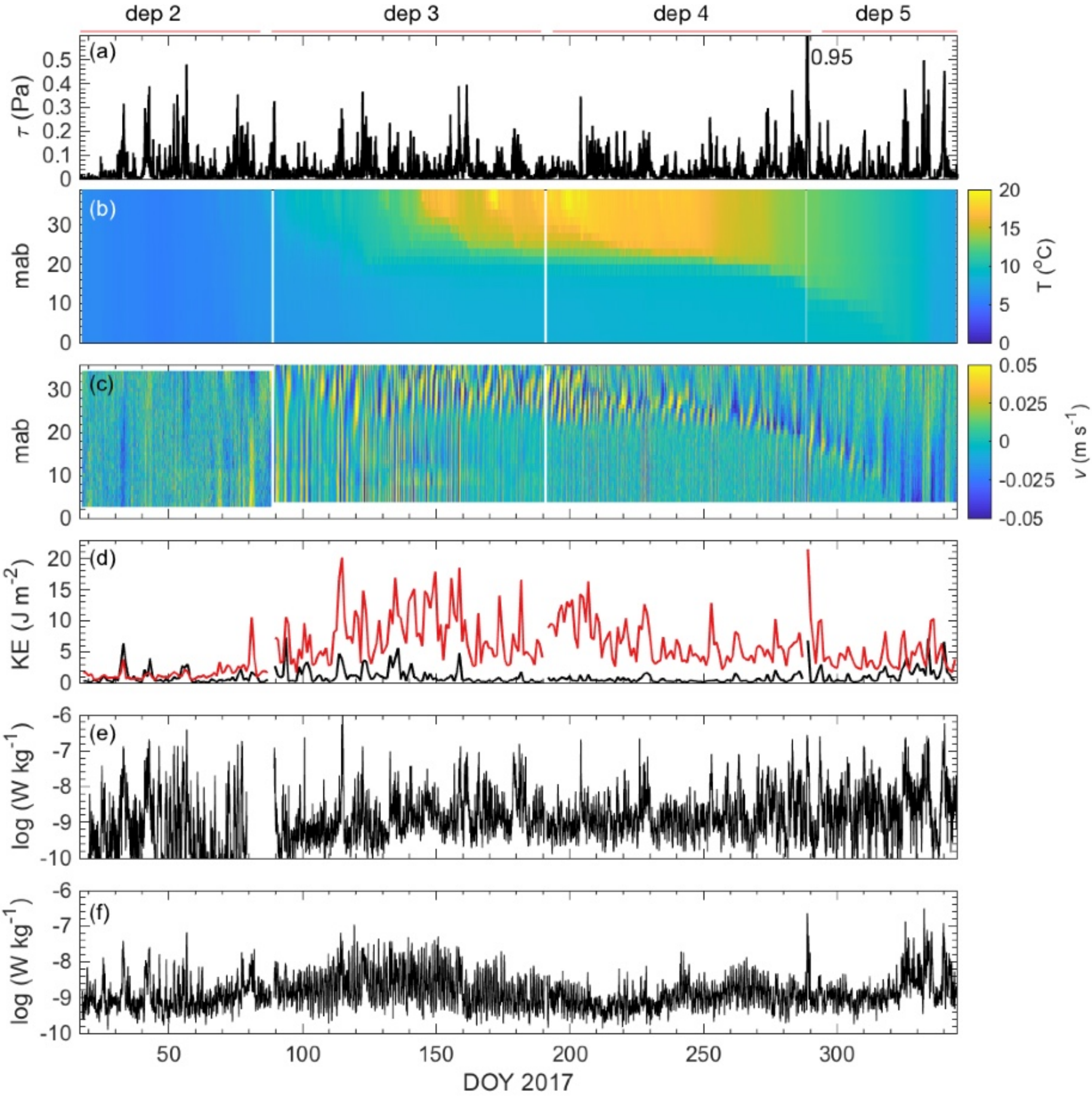
dep 2
dep 3
dep 4
dep 5
(a)
τ (Pa)
0.95
0
0.1
0.2
0.3
0.4
0.5
(b)
mab
T (°C)
0
5
10
15
20
(c)
mab
v (m s⁻¹)
0.05
0.025
0
-0.025
-0.05
(d)
KE (J m⁻²)
(e)
ε-mid
log (W kg⁻¹)
(f)
ε-BBL
log (W kg⁻¹)
-6
-7
-8
-9
-10
50
100
150
200
250
300
DOY 2017

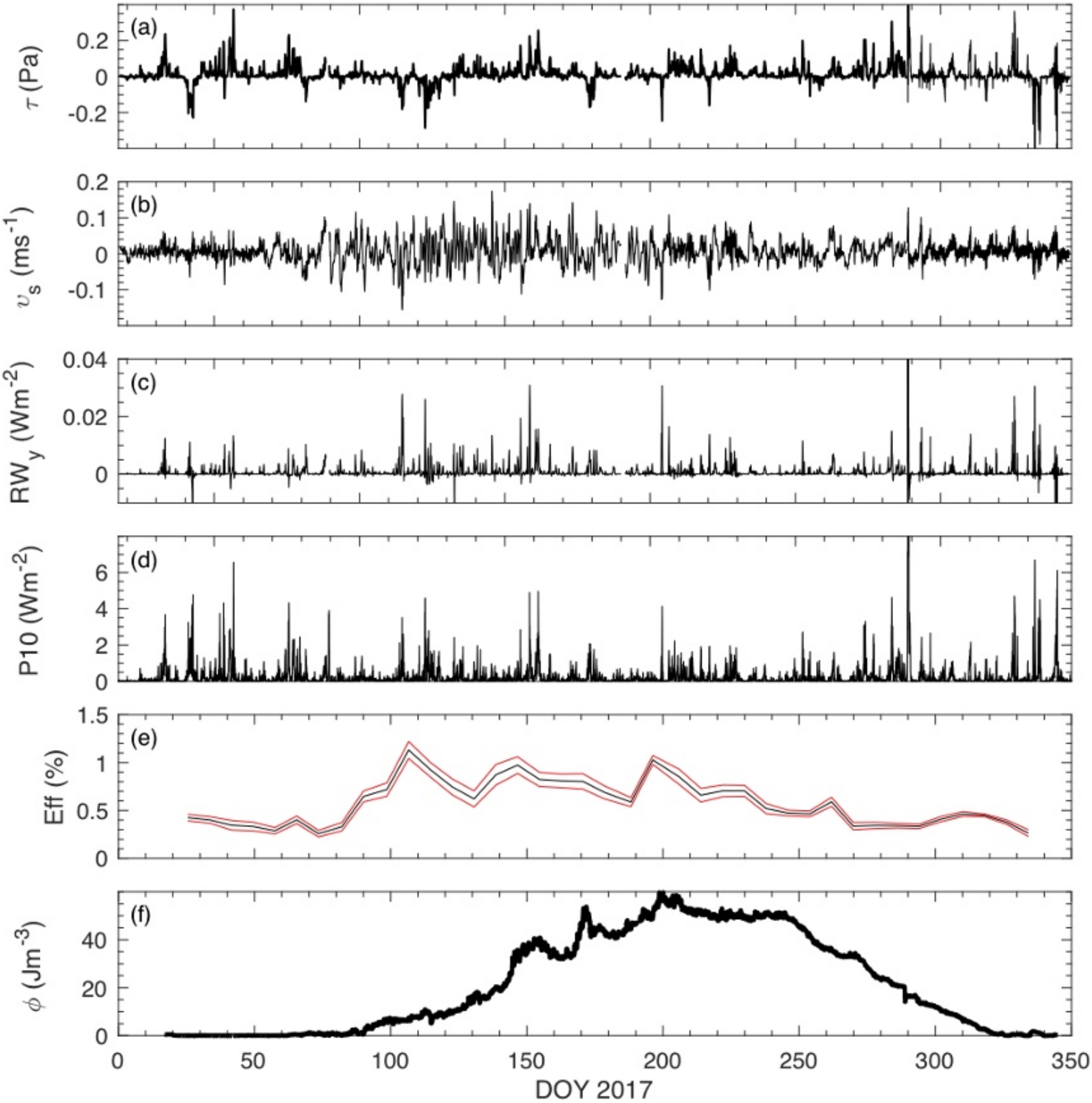
(a)
τ (Pa)
0.2
0
-0.2
(b)
v_s (ms^{-1})
0.2
0.1
0
-0.1
(c)
RW$_y$ (Wm^{-2})
0.04
0.02
0
(d)
P10 (Wm^{-2})
6
4
2
0
(e)
Eff (%)
1.5
1
0.5
0
(f)
ϕ (Jm^{-3})
40
20
0
0
50
100
150
200
250
300
350
DOY 2017

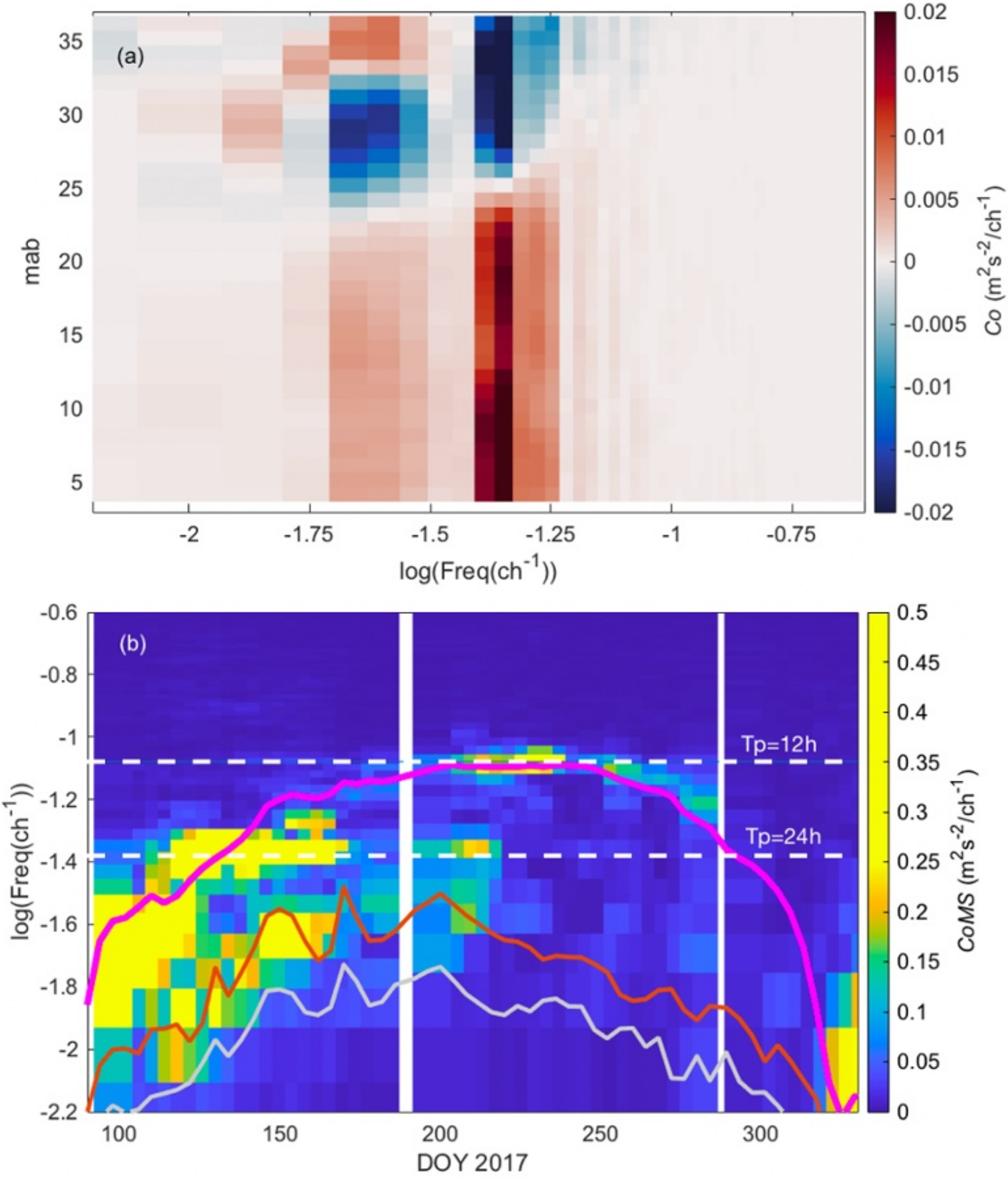
(a)
mab
35
30
25
20
15
10
5
-2
-1.75
-1.5
-1.25
-1
-0.75
log(Freq(ch^{-1}))
0.02
0.015
0.01
0.005
0
-0.005
-0.01
-0.015
-0.02
Co (m^{2}s^{-2}/ch^{-1})
(b)
log(Freq(ch^{-1}))
-0.6
-0.8
-1
-1.2
-1.4
-1.6
-1.8
-2
-2.2
Tp=12h
Tp=24h
100
150
200
250
300
DOY 2017
0.5
0.45
0.4
0.35
0.3
0.25
0.2
0.15
0.1
0.05
0
CoMS (m^{2}s^{-2}/ch^{-1})

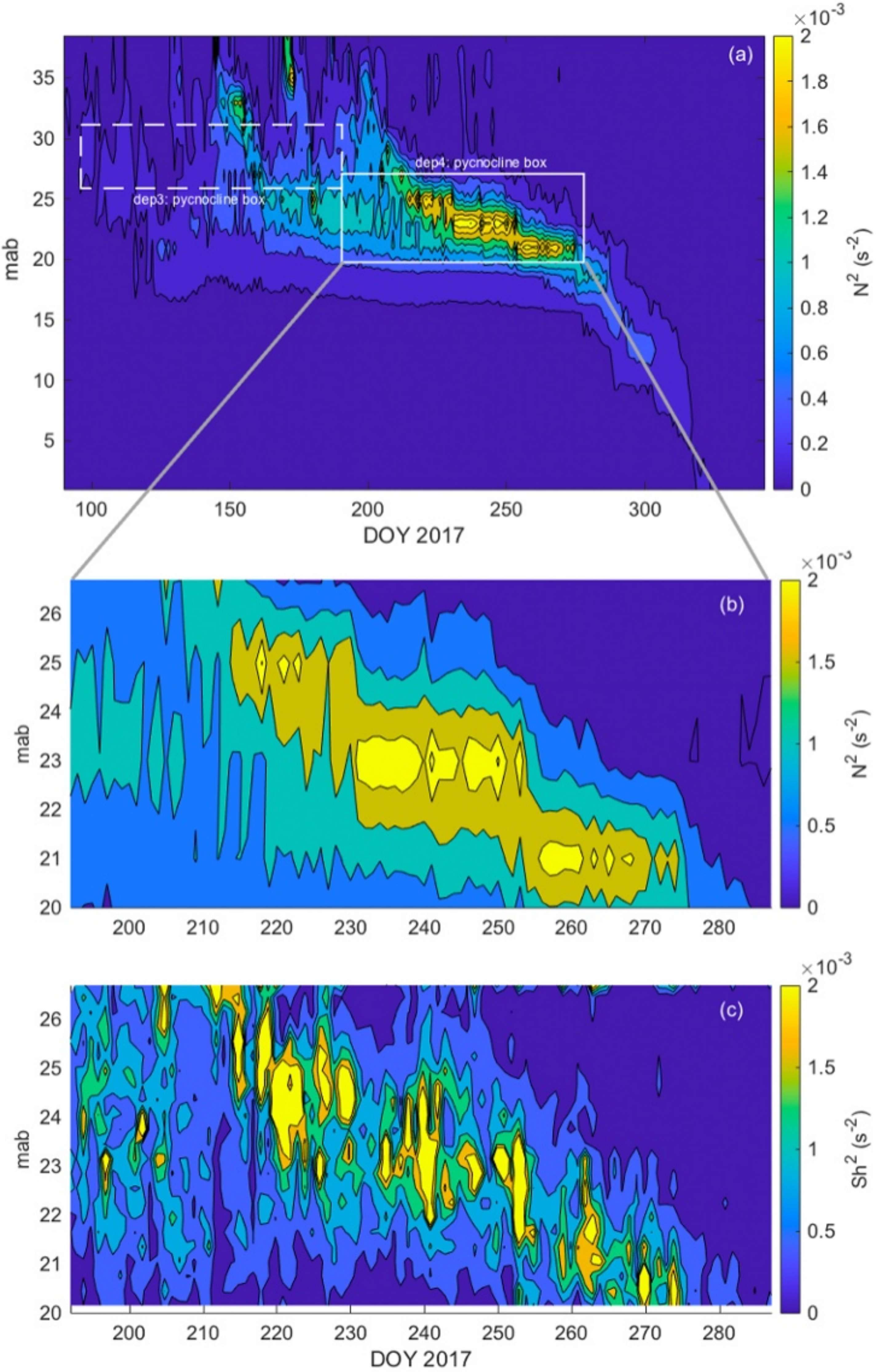
(a)
dep3: pycnocline box
dep4: pycnocline box
mab
DOY 2017
N^2 (s^{-2})
×10^{-3}
(b)
mab
DOY 2017
N^2 (s^{-2})
×10^{-3}
(c)
mab
DOY 2017
Sh^2 (s^{-2})
×10^{-3}

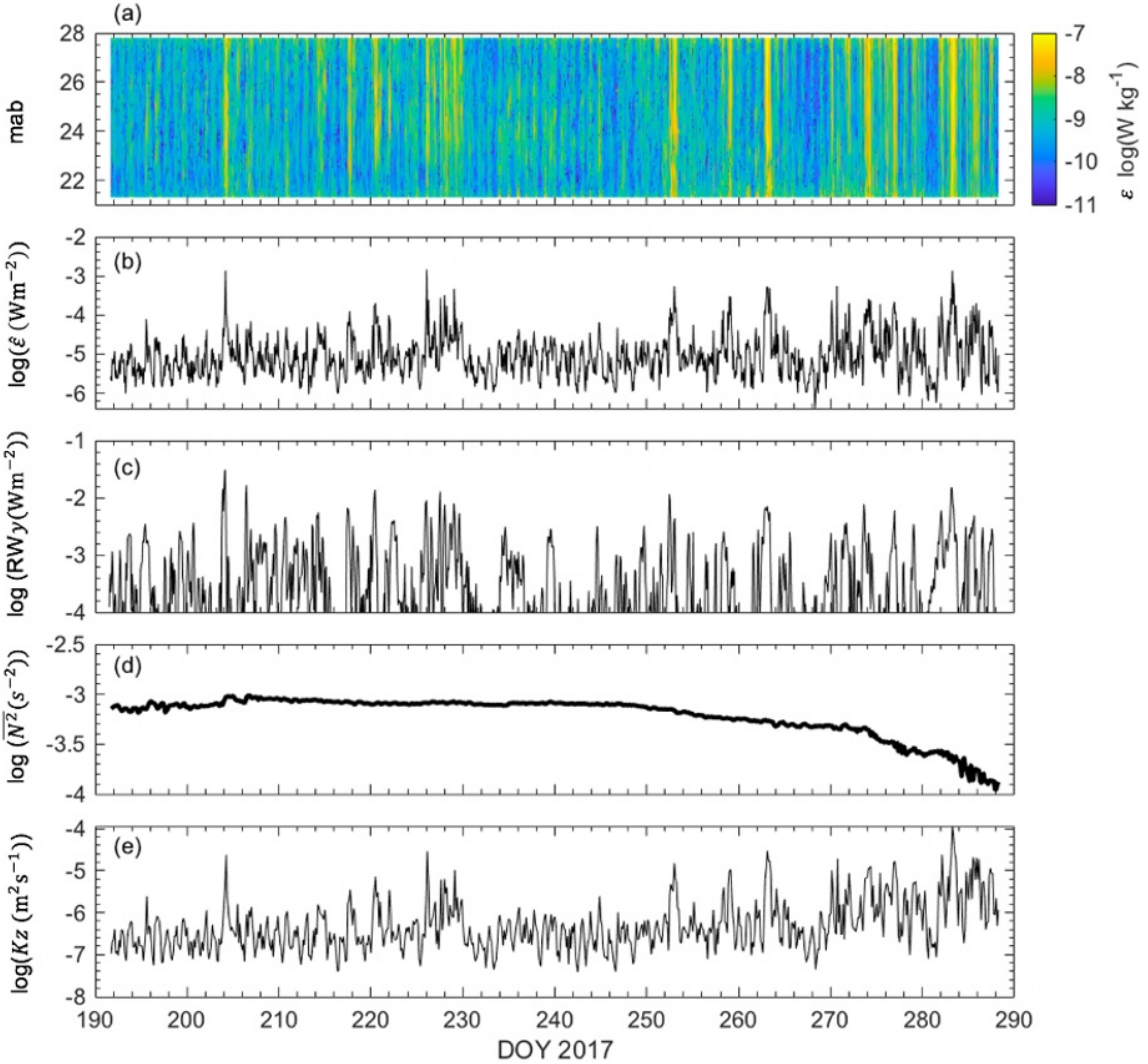
(a)
mab
28
26
24
22
-7
-8
-9
-10
-11
ε log(W kg^{-1})
(b)
log($\bar{\varepsilon}$ (Wm^{-2}))
-2
-3
-4
-5
-6
(c)
log (RWy(Wm^{-2}))
-1
-2
-3
-4
(d)
log ($\overline{N^2}$(s^{-2}))
-2.5
-3
-3.5
-4
(e)
log(Kz (m^{2}s^{-1}))
-4
-5
-6
-7
-8
190
200
210
220
230
240
250
260
270
280
290
DOY 2017

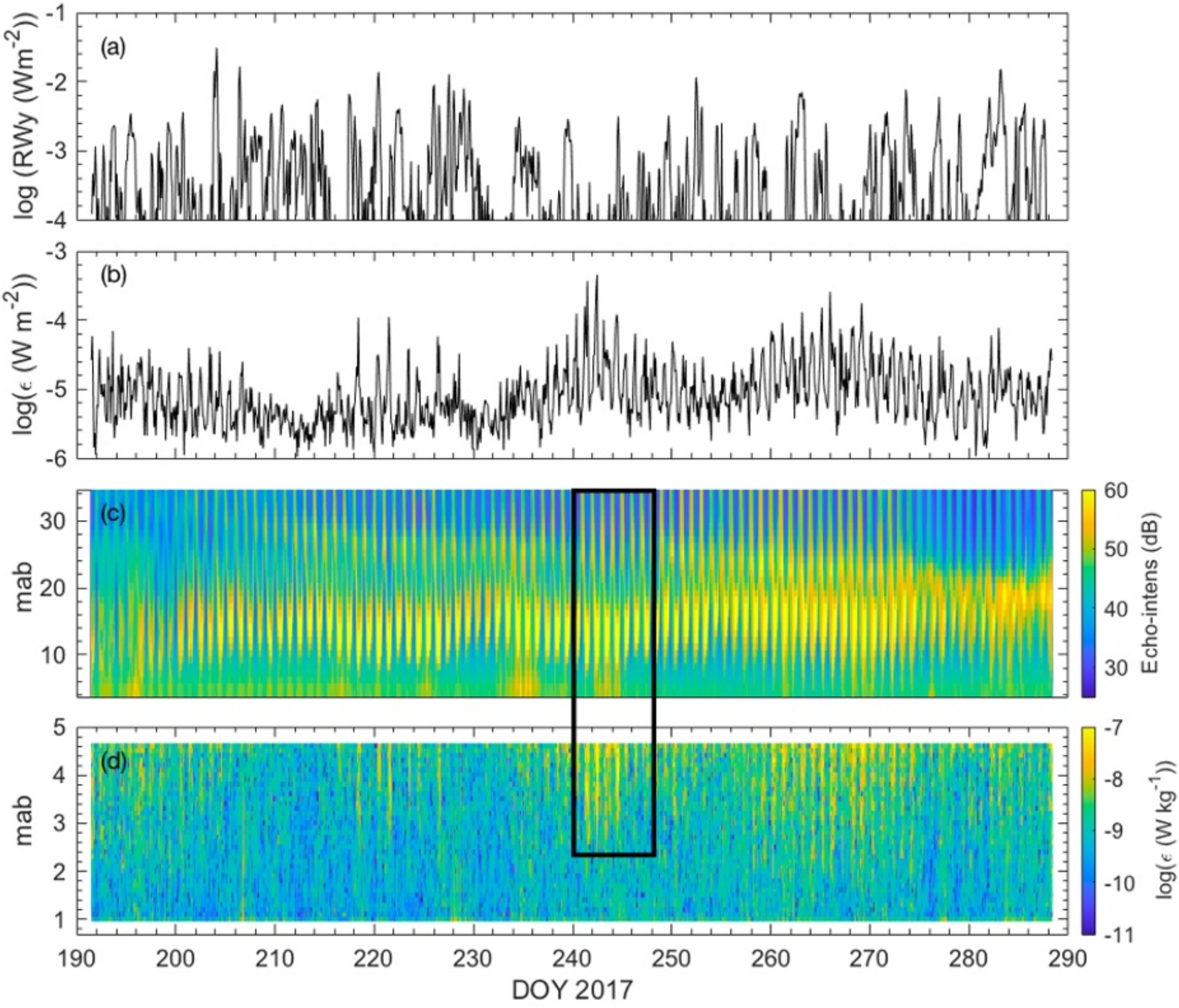
(a)
log (RWy (Wm^{-2}))
-1
-2
-3
-4
(b)
log(ϵ (W m^{-2}))
-3
-4
-5
-6
(c)
mab
30
20
10
60
50
40
30
Echo-intens (dB)
(d)
mab
5
4
3
2
1
-7
-8
-9
-10
-11
log(ϵ (W kg^{-1}))
190
200
210
220
230
240
250
260
270
280
290
DOY 2017

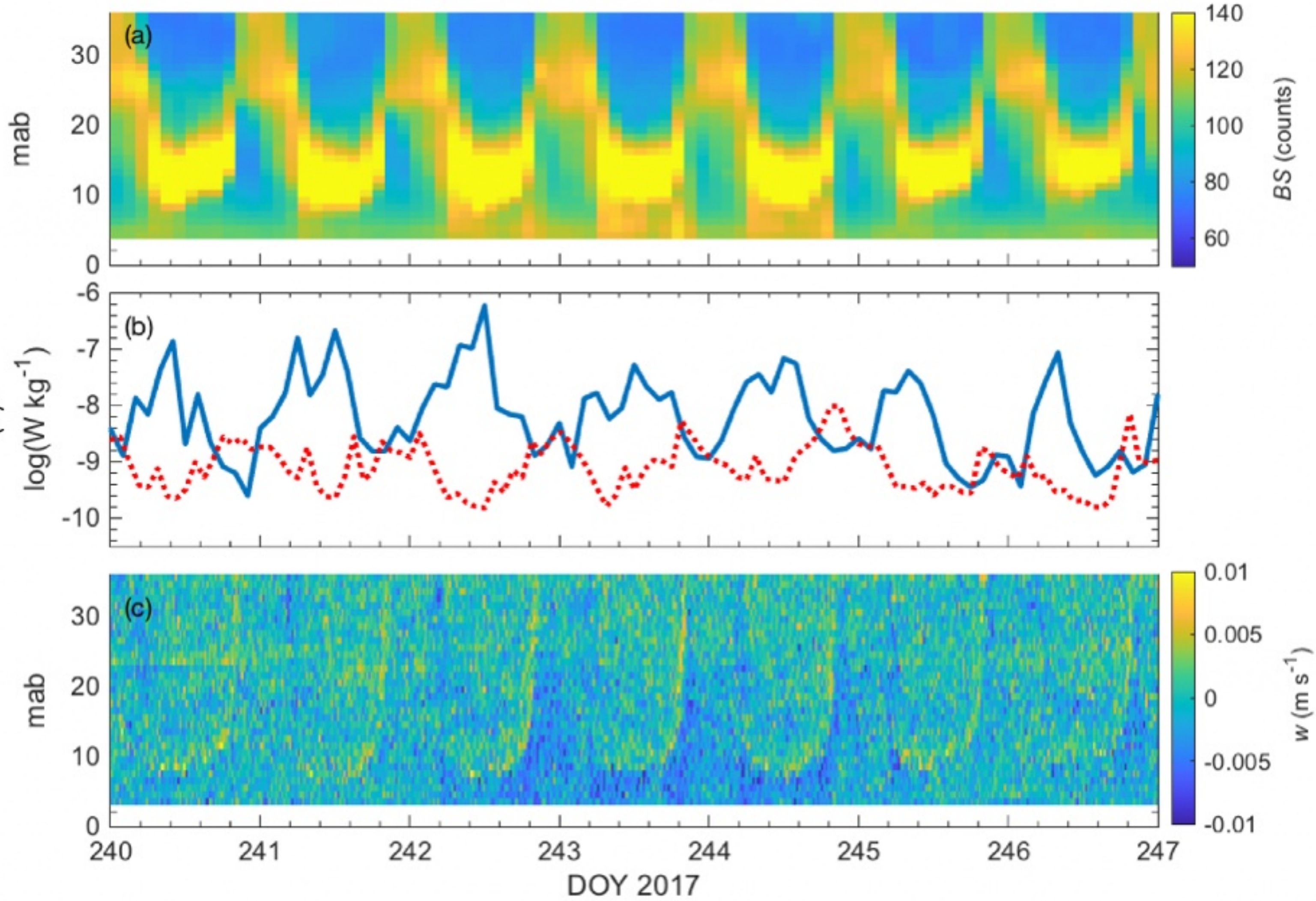
(a)
(b)
(c)
mab
30
20
10
0
140
120
100
80
60
BS (counts)
$\langle \varepsilon \rangle$
log(W kg^{-1})
-6
-7
-8
-9
-10
0.01
0.005
0
-0.005
-0.01
w (m s^{-1})
240
241
242
243
244
245
246
247
DOY 2017

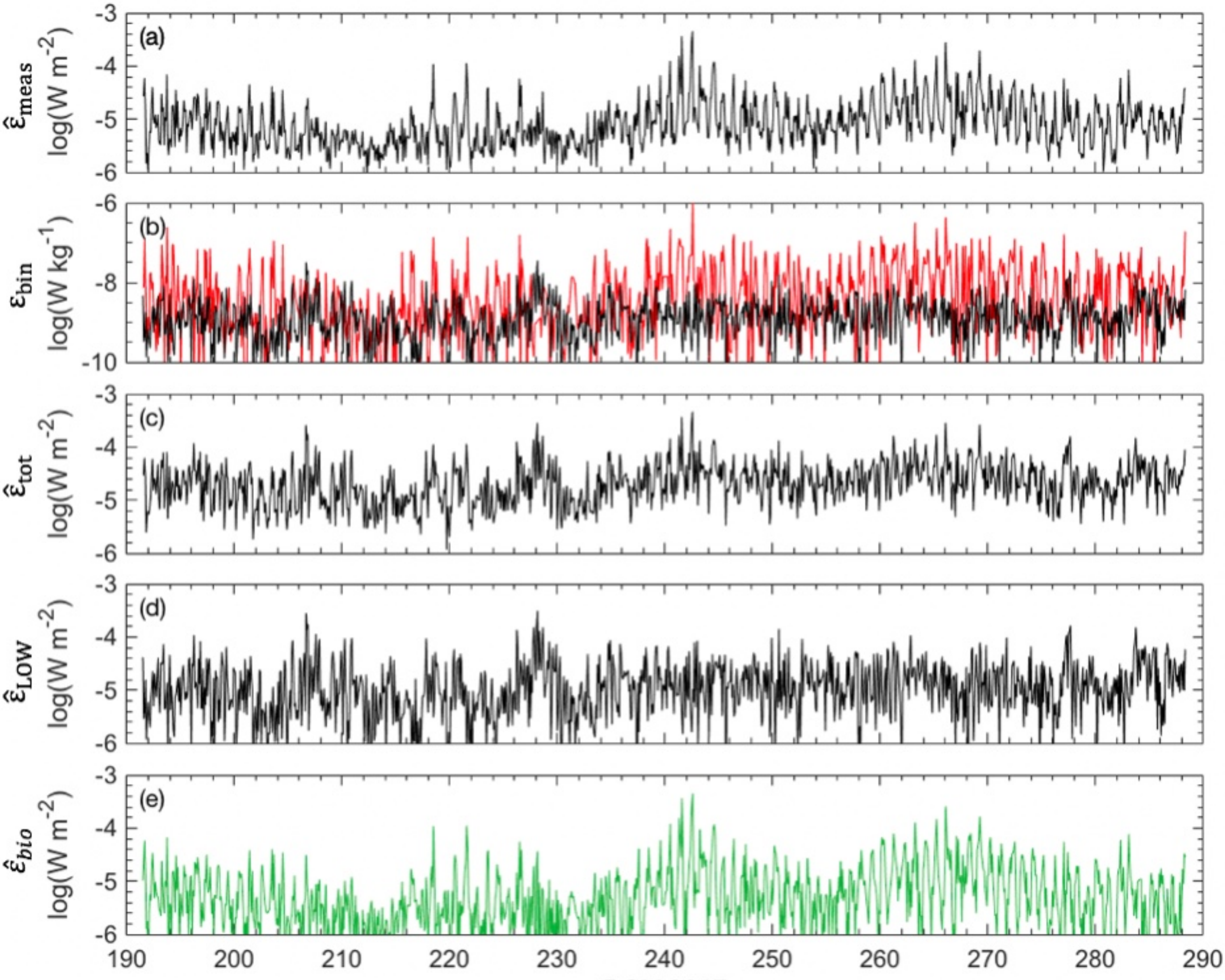
(a)
(b)
(c)
(d)
(e)
$\hat{\varepsilon}_{\mathrm{meas}}$ log(W m^{-2})
$\varepsilon_{\mathrm{bin}}$ log(W kg^{-1})
$\hat{\varepsilon}_{\mathrm{tot}}$ log(W m^{-2})
$\hat{\varepsilon}_{\mathrm{LOW}}$ log(W m^{-2})
$\hat{\varepsilon}_{bio}$ log(W m^{-2})
-3
-4
-5
-6
-8
-10
190
200
210
220
230
240
250
260
270
280
290
DOY 2017